Crystal plasticity finite element method simulation for the nano-indentation of plasma-exposed tungsten

Xiazi Xiao[a,*], D. Terentyev[b,*], A. Bakaev[b], A. Zinovev[b,c], A. Dubinko[b,d], E.E. Zhurkin[e]

[a]Department of Mechanics, School of Civil Engineering, Central South University, 410075 Changsha, P. R. China

[b]SCK•CEN, Nuclear Materials Science Institute, Boeretang 200, 2400 Mol, Belgium

[c]iMMC, Université catholique de Louvain, Av. Georges Lemaître 4, 1348 Louvain-la-Neuve, Belgium

[d]Department of Applied Physics, Ghent University, 9000 Ghent, Belgium

[e]Department of Experimental Nuclear Physics K-89, Faculty of Physics and Mechanics, St.Petersburg State Polytechnical University, 29 Polytekhnicheskaya str., 195251 St.Petersburg, Russia

Abstract

In this work, the nano-indentation of plasma-exposed tungsten is simulated by the developed crystal plasticity finite element model in the temperature range of 300-700 K. A nonlinear function is applied to characterize the depth profile of plasma-induced dislocation density in the sub-surface region. The model parameters are calibrated by comparing the simulated results with corresponding experimental data at 300 K for both the force-depth and hardness-depth relationships. Furthermore, the mechanical responses of plasma-exposed tungsten are predicted at 500 K and 700 K in order to characterize the plasma effect at the fusion-relevant operational temperature. The dominant results and conclusions are that: (1) The heterogeneously distributed dislocations in the sub-surface region induced by the plasma exposure are responsible for the increase of hardness at 300 K. (2) The plasma-induced microstructural modification does not yield to considerable increase of hardness at operational temperature. (3) The expansion of the plastic zone in the sub-surface region is, to some extent, limited by the presence of plasma-induced dislocations. Whereas, the increase of temperature can effectively reduce this limitation.

Keywords: Plasma exposure, Nano-indentation, CPFEM, Tungsten, Dislocations

*Corresponding author: xxz2017@csu.edu.cn; dterenty@sckcen.be

1. Introduction

Tungsten and its alloys have been extensively studied over the last decade [1-7] since tungsten is the main candidate for armour materials in the plasma facing components for future nuclear fusion reactors. Its selection is driven by the superior thermal properties, high melting temperature, high thermal conductivity [8], low tritium retention [9, 10] and low sputtering yield [11]. The application of tungsten, however, has certain restrictions concerning its neutron irradiation tolerance [12]. A full tungsten divertor is designed for ITER, the largest fusion reactor under construction, and it is also a promising plasma-facing candidate material for the Demonstration Power Plant Reactor (DEMO) [13, 14].

Despite a number of promising characteristics, the interaction of tungsten with high flux plasma remains an important problem to explore. It is known that the thermal stresses as well as the permeation of the plasma components combined with cyclic loads cause surface cracking [15-17], which is especially dangerous during transient heat loads [18-20]. While the direct penetration of plasma ions is limited to a tiny sub-surface layer (the kinetic penetration of plasma ions is within a few nanometers), the thermal stresses extend to tens of micro-meters [21]. Overall, the presence of thermal stresses causes the nucleation and propagation of macro-cracks through the material, which is why it is important to understand the moment of crack initiation that occurs at a shallow depth.

The dedicated transmission electron microscope (TEM) studies were performed recently to assess the sub-surface microstructure of tungsten exposed to high flux plasma mimicking ITER divertor operational conditions [22-26]. It was found that the main impact of plasma exposure is expressed in a strong increase of dislocation density, which is limited to a depth of ~10 µm. This intensive plastic deformation could act as the predecessor of crack nucleation. Nano-indentation (NI) experiments have also revealed the increase of the surface hardness in this region [27-29]. The hardening induced by plasma exposure was attributed to the pinning of gliding dislocations by the existing dislocation network and nano-metric bubbles. Moreover, a recent work [30] has revealed that plasma exposure results in a decrease of the pop-in load and at the same time an increase of hardness, which is another indicator of the embrittlement effect induced by the plasma [31].

The above mentioned works also highlight the role of micro-scale testing offered by NI, which is a unique technique for the presented problem since the conventional mechanical test approaches (e. g. uniaxial tensile or Vickers hardness tests) are not applicable due to the very small space scale of the phenomenon of concern [32-34]. However, the direct output of NI measurements requires post-processing and interpretation to deduce the conventional mechanical properties. This is why the modelling of NI process and deduction of corresponding constitutive properties are becoming a hot topic in the computational studies [35-40].

In this work, we continue the investigation of tungsten and perform the computational assessment of the experimental results reported earlier by means of NI [41]. In particular, we apply the crystal plasticity finite element method (CPFEM) to simulate the NI response at room temperature of IGP tungsten (ITER-grade W manufactured by Plansee SE, Austria) exposed to the high flux plasma, and predict the expected response at operational temperature (up to 700 K). The main purpose of the study is to clarify how strong is the impact of the highly localized sub-surface plastic deformation (as a result of the plasma exposure) on the mechanical deformation of tungsten during the NI process.

2. Methodology and experimental techniques

2.1 Experiments

The samples of 10×10×1 mm^3 were cut from a bar of commercially pure tungsten of 99.97% purity. The production route and initial microstructure of the material are reported in our previous studies [42]. The reference microstructure of the material is characterized by dislocation density in the range of 4∼8×10^{12} m^{-2}, as measured by TEM, and the grain size equals to 5∼20 µm normal to the bar axis and 50∼100 µm along the bar axis, as measured by scanning electron microscopy (SEM) and electron back scattering diffraction (EBSD). The sub-grains are also present in the material, and their typical size varies from 0.6 to 1.7 µm normal to the bar axis and 2.3∼4 µm along the bar axis. The samples for plasma exposure and subsequent NI testing were cut with the help of electrical discharge machining (EDM), and then polished down to 0.25 µm to reach the mirror surface level.

The exposures were performed in linear plasma generator Pilot-PSI [43], which delivers the high-density deuterium (D) plasma beam to simulate the plasma-wall interaction conditions expected in the divertor of ITER. The ion energy was ~50 eV. The full width at half maximum of the beam was ~10 mm thus ensuring rather small gradients of temperature and flux at the sample's surface. The surface temperature during the exposure was 470 ±10 K, as measured by an infra-red camera. The particle flux was ~10^{24} D/m^2/s, calculated from the plasma electron density and electron temperature, as measured by Thomson scattering [44]. The total fluence was equal to 4×10^{26} D/m^2.

The exposed and reference samples were tested using the Agilent G200 nanoindenter at room temperature in the continuous stiffness mode (CSM) [45] with the standard XP head equipped with a Berkovich diamond tip. The oscillation amplitude and frequency were 2 nm and 45 Hz, respectively. The tip area function was calibrated by performing a series of indents in a reference fused silica sample. The indentation strain rate was set to be 0.05 s^{-1}, and the specimens were indented down to a penetration depth h_{NI}=1.5 µm. Several areas with 25 indents each were probed. The indents were spaced by a distance of 60 µm. The hardness was calculated using the classical Oliver & Pharr method [45].

2.2 CPFEM for the NI of plasma-exposed tungsten

Recently, the current authors have developed a CPFEM model to simulate the NI mechanical test of as-received (pristine) polycrystalline tungsten in the temperature range of 300-691 K [40]. Three dominant hardening mechanisms were considered in the model for the thermo-mechanical deformation of tungsten, including the lattice friction stress τ_{LF}, Hall-Petch hardening term τ_{HP} and dislocation hardening term τ_{SSD}. By comparing the simulated results with experimental data for both the force-depth and hardness-depth relationships, a reliable set of model parameters has been obtained so that the simulated results could match well with corresponding experimental data. In this work, the calibrated constitutive equations are further applied to simulate the NI process of plasma-exposed tungsten in the temperature range of 300-700 K.

Being different from the homogeneously distributed dislocations in the as-received tungsten, the initial distribution of microstructure in the sub-surface of plasma-exposed tungsten can be dramatically modified due to the intensive plastic deformation during the plasma exposure process. A typical distribution of the dislocation density as a function of depth is illustrated in Fig. 1(a) for IGP tungsten, which was exposed by pure D plasma at 470 K with the fluence of up to 4×10^{26} D/m^2 [41]. The dislocation density decreases from 5.34×10^{13} m^{-2} in the surface region down to 0.30×10^{13} m^{-2} in the bulk region. The depth of the plasma affected region is about 15 μm. In order to continuously characterize the initial distribution of dislocation density in the α-th slip system, the following logistic function is applied to best fit the experimental data:

$$\rho^{\alpha}_{\mathrm{SSD}}(h) = A_1 + \frac{A_2}{1+(h/h_0)^p} \tag{1}$$

where A_1, A_2 and p are the fitting parameters, and h_0 is the reference depth. Then Eq. (1) can be substituted into the dislocation hardening term:

$$\tau^{\alpha}_{\mathrm{SSD}}(T,h) = \mu(T) b h_{\mathrm{SSD}}(T)\sqrt{\rho^{\alpha}_{\mathrm{SSD}}(h)} \tag{2}$$

where μ, b and h_{SSD} are, respectively, the shear modulus, Burgers vector value and dislocation strength coefficient. As indicated in Eq. (2), the initial distribution of $\tau^{\alpha}_{\mathrm{SSD}}$ with plasma effect not only depends on the distance from the sample surface *h*, but also is a function of the testing temperature T. In Fig. 1(b), a typical distribution of $\tau^{\alpha}_{\text{SSD}}$ is illustrated corresponding to the distribution of dislocation density as given in Fig. 1(a) when T=300 K. In this case, $A_1 = 0.30\times10^{13}$ m^{-2}, $A_2 = 5.03\times10^{13}$ m^{-2}, $h_0 = 4.34$ μm and $p = 2.51$ are the fitting parameters in Eq. (1) for the mean value of experimental data [41]. Note that our model is based on the assumption that the dislocation density depth profile does not depend on the plasma-exposure temperature.

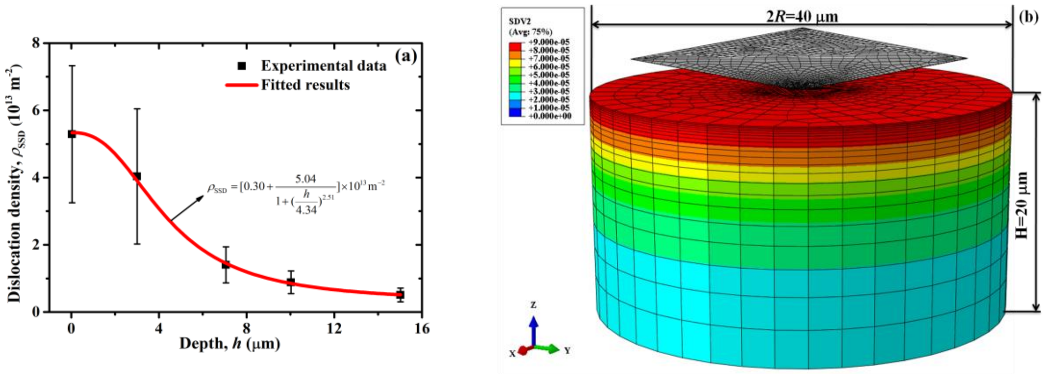

Fig. 1. (a) The initial distribution of dislocation density in IGP W after the pure D plasma exposure at 470 K and the fluence up to 4×10^{26} D/m^2 [41]. (b) The initial distribution of τ_{SSD} at 300 K (measured in TPa) corresponding to the distribution of dislocation density as illustrated in Fig. 1(a).

Besides the dislocation hardening term, the two remaining hardening mechanisms (i.e. τ_{LF} and τ_{HP}) as well as the strain hardening evolution law are assumed to be unaffected by the plasma exposure, therefore, the core of the crystal plasticity model developed in our previous work [40] still hold. The fundamental constitutive equations characterizing the plastic deformation of plasma-exposed tungsten are summarized in Table 1. More details on the derivation of the theoretical model are presented in our previous work [40].

Table 1. The fundamental constitutive equations for plasma-exposed tungsten with temperature effect.

Definition	Expression	Function	Description

Critical resolved shear stress (CRSS)	$\tau_{\mathrm{CRSS}}^{\alpha}(T,h)$	$\tau_{\mathrm{LF}}(T)+\tau_{\mathrm{HP}}(T)+\tau_{\mathrm{SSD}}^{\alpha}(T,h)$	Three hardening terms contribute to the CRSS in the α-th slip system
Lattice friction stress	$\tau_{\mathrm{LF}}(T)$	$\begin{cases}\tau_{\mathrm{p0}}\left[1-\sqrt{\dfrac{k_{\mathrm{B}}T}{2H_{\mathrm{k}}}\ln\left(\dfrac{\dot{\gamma}_{\mathrm{p0}}}{\dot{\varepsilon}}\right)}\right], T\le T_0 \\ \tau_{\mathrm{f0}}\left[1-\dfrac{k_{\mathrm{B}}T}{2H_{\mathrm{k}}}\ln\left(\dfrac{\dot{\gamma}_{\mathrm{p0}}}{\dot{\varepsilon}}\right)\right]^2, T>T_0\end{cases}$	$\tau_{\mathrm{LF}}(T)$ indicates the thermally-activated motion of screw dislocations
Hall-Petch hardening term	$\tau_{\mathrm{HP}}(T)$	$k_{\mathrm{HP}}(T)d^{-0.5}$	$\tau_{\mathrm{HP}}(T)$ characterizes the hardening effect of grain boundaries
Dislocation hardening term	$\tau_{\mathrm{SSD}}^{\alpha}(T,h)$	$\mu(T)bh_{\mathrm{SSD}}(T)\sqrt{\rho_{\mathrm{SSD}}^{\alpha}(h)}$	$\tau_{\mathrm{SSD}}^{\alpha}(T,h)$ with plasma effect is a function of *T* and *h*
Evolution of the CRSS	$\dot{\tau}_{\mathrm{CRSS}}^{\alpha}(T,h)$	$\sum_{\beta=1}^{N_{\mathrm{s}}} H^{\alpha\beta}(T,h)\lvert\dot{\gamma}^{\beta}\rvert$	Evolution of dislocation density in different slip systems contributes to the evolution of CRSS

To be consistent with the experimental setup, a Berkovich indenter is used in our CPFEM model to penetrate the plasma-exposed tungsten. The constitutive equations are implemented into the subroutine VUMAT of Abaqus. The geometrical model of the indented sample is a cylinder with the radius of 20 μm and height of 20 μm as illustrated in Fig. 1(b). The meshed cylinder contains 32676 linear hexahedral elements of the type C3D8R and 34386 nodes, and the indenter is taken as a rigid body. The mesh is refined in the region beneath the indenter tip with the minimum size of 0.2 μm and 0.1 μm in the x-y plane and z axis direction, respectively. Only the bottom of the cylinder is fixed, and the frictionless interaction is applied between the sample surface and indenter tip [40].

3. Results and discussions

In this work, the developed CPFEM model is applied to simulate the NI process of plasma-exposed tungsten in the temperature range of 300-700 K. The numerical results at 300 K are firstly compared with experimental data to validate the calibrated theoretical model. Then, the mechanical responses at 500 K and 700 K are predicted to derive the temperature effect on the increase of hardness of the plasma-exposed tungsten. Moreover, the plasma and temperature effects on the distribution of the equivalent plastic strain (PEEQ in Abaqus' terms) and von Mises stress are addressed to better understand the fundamental deformation mechanisms.

3.1 Force-depth and hardness-depth relationships

By applying the same set of parameters as listed in Table 1 of our previous work [40], the NI test of IGP tungsten unexposed and exposed to plasma has been simulated with the CPFEM model. Analysis of an EBSD image of IGP tungsten before plasma exposure indicated that the main crystallographic orientations of grains are <111>, <101> and <212>, occupying 15%, 20% and 60% of the image area, respectively. Then, a series of CPFEM simulations of NI at 300 K along the above mentioned directions was performed, and the average of the force-depth relationships along these directions with corresponding weights is approximately taken as the mechanical response of polycrystalline tungsten. In order to validate the parameterized model, the simulated force-depth relationships with and without plasma effect are compared with the corresponding experimental data at 300 K. As shown in Fig. 2(a), a reasonable match is realized when applying the following input parameters: $\rho^{\alpha}_{\mathrm{SSD}}(h) = 1\times10^{10}$

m^{-2} for the as-received tungsten [40] and $\rho_{\mathrm{SSD}}^{\alpha}(h) = A_1 + \dfrac{A_2}{1+(h/h_0)^p}$ with $A_1 = 0.30\times10^{13}$ m^{-2}, $A_2 = 5.03\times10^{13}$ m^{-2}, $h_0 = 4.34$ μm and $p = 2.51$ for the plasma-exposed tungsten.

With the obtained force-depth relationship, the hardness as a function of the indentation depth can be calculated as $H = F/A$, where F is the loading force and A is the contact area. The latter parameters were calculated using the expressions: A=$24.56h_{\mathrm{c}}^2$ (for the Berkovich indenter) and $h_{\mathrm{c}} = h - k \cdot F/(\mathrm{d}F/\mathrm{d}h)$ wtih $k = 0.75$ [46]. The calculated hardness-depth relationships with and without plasma effect at 300 K are illustrated in Fig. 2(b). As one can see, the hardness of unexposed IGP tungsten at room temperature is about 6 GPa when the indentation depth ranges from 500 nm to 1000 nm. Whereas, the hardness of the plasma-exposed tungstenis is slightly higher than that of the as-received tungsten for the same test temperature. To be specific, an obvious increase of hardness ΔH is noticed at 300 K as shown in Fig. 2(c), and the simulated results show a good agreement with the experimental data. With the increase of indentation depth h, ΔH value decreases from ~0.48 GPa at 500 nm down to ~0.26 GPa at 1000 nm due to the heterogeneously-distributed dislocations in the sub-surface region as illustrated in Fig. 1(a).

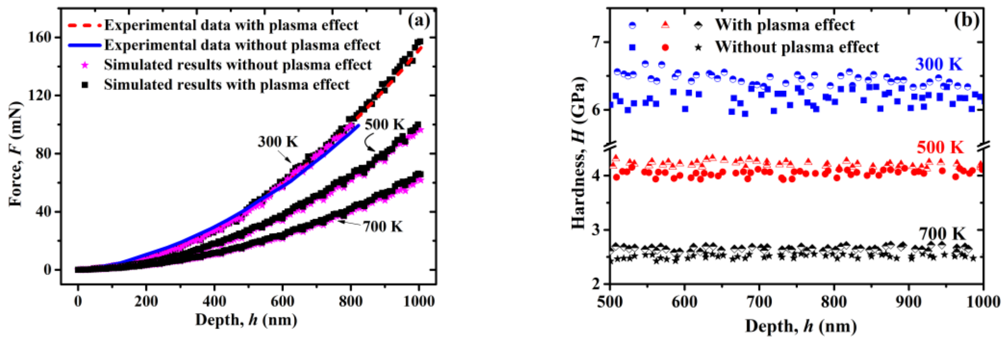

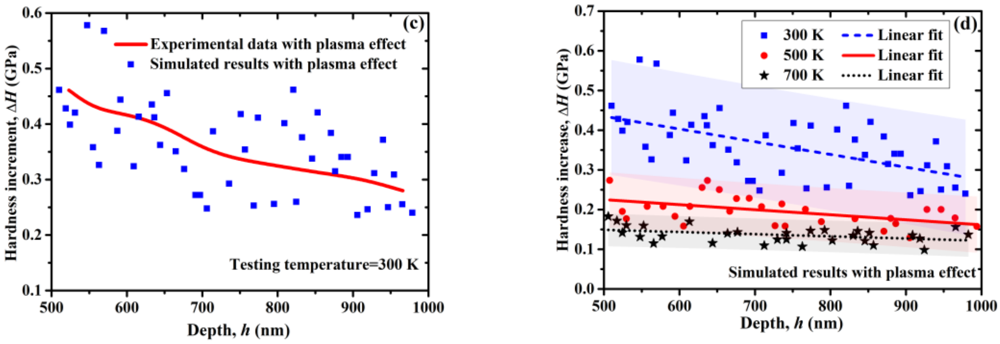

Fig. 2. (a) The experimental data (lines) and simulated NI results (dots) are compared for the $F-h$ relationship of plasma-exposed IGP tungsten when the testing temperatures are 300 K, 500 K and 700 K. (b) The simulated $H-h$ relationships with and without plasma effect are compared for the different testing temperatures. (c) The $\Delta H-h$ relationship is compared between the experimental data and simulated results when the testing temperature is 300 K. (d) The simulated $\Delta H-h$ relationship is compared when the testing temperature are 300 K, 500 K and 700 K. The linear fit for each set of simulated results and 95% prediction bands are also added.

After the validation of the parameterized constitutive equations, the developed CPFEM model was further applied to predict the mechanical response of IGP tungsten at operational temperature. As compared in Fig. 2(a) and (b), the increase of temperature results in the decrease of the strength of tungsten: the hardness without plasma effect decreases from ~6 GPa at 300 K down to ~4 GPa at 500 K and ~2 GPa at 700 K. The dominant reason for this decrease originates from the decrease of τ_{LF}, τ_{HP} and τ_{SSD} at high temperature. The temperature effect on ΔH is demonstrated in Fig. 2(d). Considering the dislocation hardening term as expressed in Eq. (2), the increase of temperature leads to the decrease of both the shear modulus μ and dislocation hardening coefficient h_{SSD}, therefore, ΔH, which is primarily a result of the plasma-induced dislocation formation, tends to decrease with the increase of temperature.

In order to further analyze the influence of the initial distribution of dislocation density on the $\Delta H-h$ relationship, three distribution functions are considered, which, respectively, characterize the upper boundary $\rho_{\mathrm{SSD}}^{\mathrm{up}}$, mean value $\rho_{\mathrm{SSD}}^{\mathrm{mean}}$ and lower boundary $\rho_{\mathrm{SSD}}^{\mathrm{low}}$ of the experimental data [41] as illustrated in Fig. 3(a). The corresponding fitting parameters in the expression of Eq. (1) are listed in Table 2. The numerical results are compared in Fig. 3(b) and (c), and one can clearly observe that the variation of ρ_{SSD} has a limited influence on the $F-h$ relationship, whereas, the $\Delta H-h$ relationship seems to offer an effective way to assess the influence of the microstructure modification on the mechanical response of plasma-exposed tungsten, i.e. the effect of the decrease of ρ_{SSD} on the decrease of ΔH at a given h.

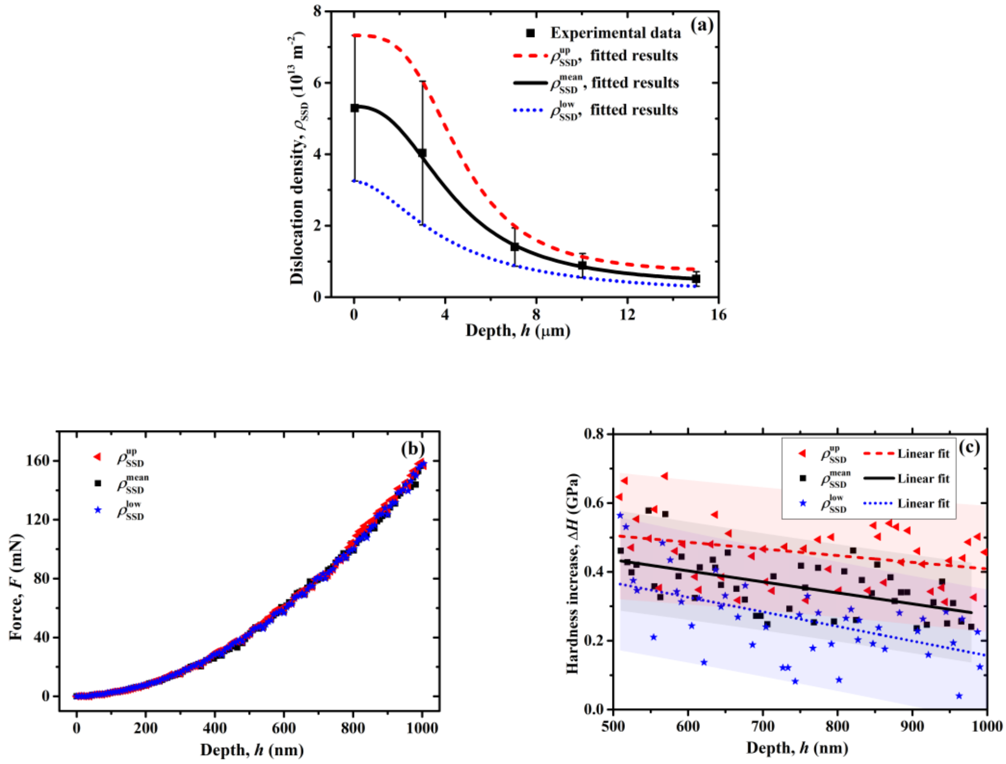

Fig. 3. (a) The dislocation density depth profile with different fitting functions for the upper boundary ($\rho_{\mathrm{SSD}}^{\mathrm{up}}$, dashed line), mean value ($\rho_{\mathrm{SSD}}^{\mathrm{mean}}$, solid line) and lower boundary ($\rho_{\mathrm{SSD}}^{\mathrm{low}}$, dotted line) of experimental data [41]. (b) The simulated $F-h$ relationship for three distributions of dislocation density, i.e. $\rho_{\mathrm{SSD}}^{\mathrm{up}}$, $\rho_{\mathrm{SSD}}^{\mathrm{mean}}$ and $\rho_{\mathrm{SSD}}^{\mathrm{low}}$. (c) The simulated $\Delta H-h$ relationship for three distributions of dislocation density, i.e. $\rho_{\mathrm{SSD}}^{\mathrm{up}}$, $\rho_{\mathrm{SSD}}^{\mathrm{mean}}$ and $\rho_{\mathrm{SSD}}^{\mathrm{low}}$. The linear fit for each set of simulated results and 95%

prediction band are also added.

Table 2. Fitting parameters in the expression of Eq. (1) for the upper boundary, mean value and lower boundary of experimental data [41].

	A_1 ($\times 10^{13}$ m^{-2})	A_2 ($\times 10^{13}$ m^{-2})	h_0 (μm)	p
$\rho_{\mathrm{SSD}}^{\mathrm{up}}$	0.64	6.68	4.64	3.31
$\rho_{\mathrm{SSD}}^{\mathrm{mean}}$	0.30	5.03	4.34	2.51
$\rho_{\mathrm{SSD}}^{\mathrm{low}}$	0.03	3.23	4.00	1.79

3.2 Temperature and plasma effects on hardening mechanisms, equivalent plastic strain and the von Mises stress

After the analysis of the macroscopic mechanical responses of polycrystalline tungsten with and without plasma effect, in this subsection, the temperature and plasma effect on the hardening mechanisms, PEEQ and von Mises stress are addressed to help obtain a sophisticated deformation mechanism related to the $F-h$ and $\Delta H-h$ relationships.

Fig. 4 illustrates the temperature and plasma effects on τ_{SSD}, τ_{LF} and τ_{HP}. For polycrystalline tungsten without plasma effect, τ_{LF} and τ_{HP} are nearly three orders of magnitude higher than τ_{SSD} when the temperature ranges from 300 K to 700 K, which indicates that the lattice friction and grain boundary effect are the dominant hardening mechanisms for IGP tungsten without plasma effect. After plasma exposure, numbers of dislocations are generated in the sub-surface region, which lead to the increase of τ_{SSD} by nearly two orders of magnitude. One should note that the plasma-induced ρ_{SSD} is inhomogeneous in the sub-surface region, therefore, τ_{SSD} gradually decreases with the increase of h at different temperatures. It is the heterogeneously distributed dislocations in the sub-surface region that result in the decrease of ΔH with h as illustrated in Fig. 2(c). Whereas, the increase of hardness is quite limited as τ_{LF} and τ_{HP} are still the dominant hardening mechanisms even in the plasma-exposed tungsten.

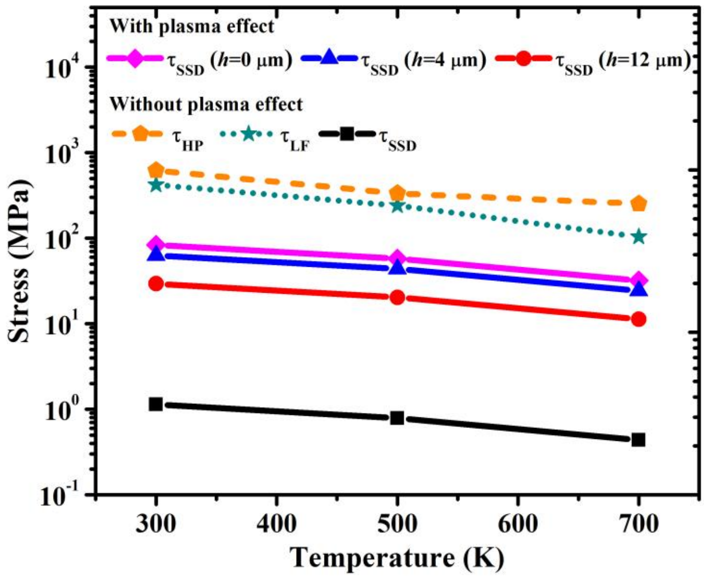

Fig. 4. The temperature and plasma effects on τ_{SSD}, τ_{LF} and τ_{HP}. For plasma-exposed tungsten τ_{SSD} is shown for the depths equal to *h*=0 μm, *h*=4 μm and *h*=12 μm.

The plasma and temperature effects on the distribution of PEEQ are compared in the cross-section of the indented sample as shown in Fig. 5. The indentation depth is 750 nm, and the loading direction is along [212]. It can be seen that: (1) With and without plasma effect, the area of the PEEQ (S_{PEEQ}) increases with temperature, which originates from the weakened slip resistance of dislocations at high temperature. (2) For a given temperature, S_{PEEQ} with plasma effect is smaller than that without plasma effect, which mainly comes from the obstruction of dislocation glide due to the increase of dislocation density in the sub-surface region. (3) S_{PEEQ} with and without plasma effect at different temperatures is summarized in Table 3. The relative difference of S_{PEEQ} with and without plasma effect gradually decreases with the increase of temperature, which indicates that the plasma effect on the expansion of the plastic zone diminishes at high operational temperature.

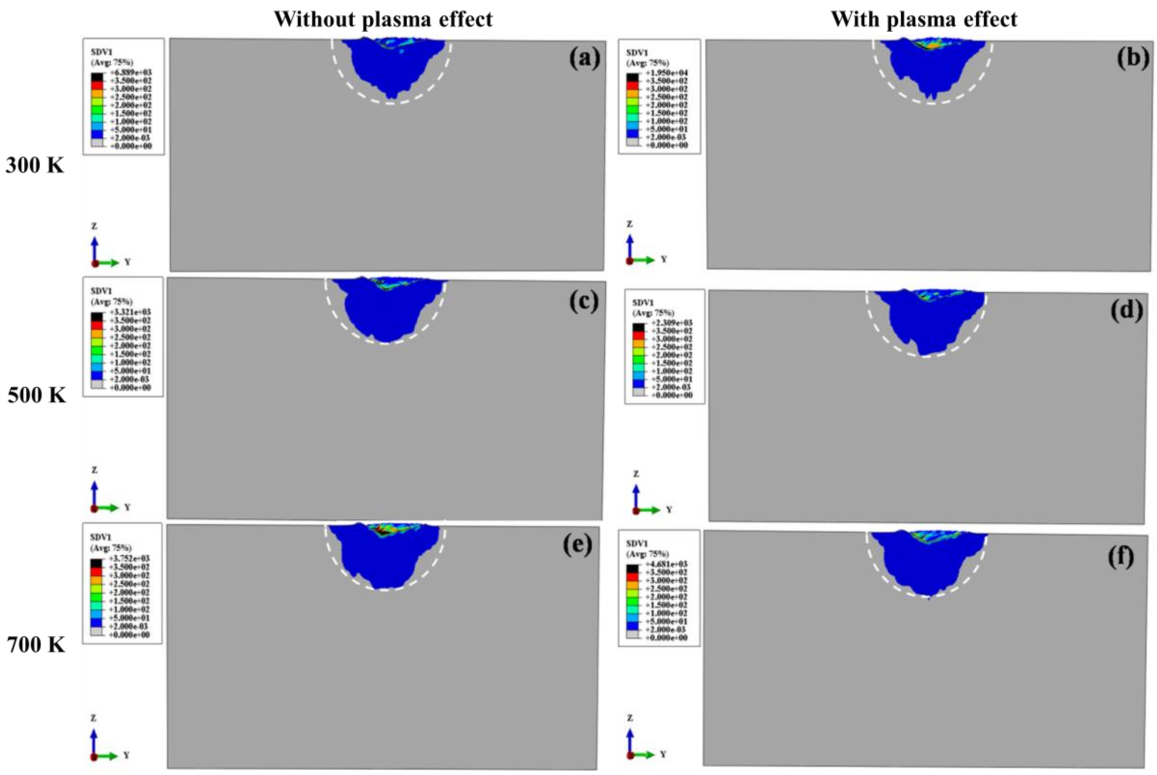

Fig. 5. The effects of plasma and temperature on the distribution of PEEQ. The indentation depth is 750 nm, and the loading direction is along [212]. The hemisphere with dashed lines is of the same radius in all six figures.

Table 3. The area of the PEEQ region (S_{PEEQ}) as illustrated in Fig. 5.

Reference		Plasma-exposed		Relative difference, %
Fig. 5	S_{PEEQ} (μm^2)	Fig. 5	S_{PEEQ} (μm^2)	
a	28.9	b	26.1	-10.7
c	35.9	d	34.8	-3.1
e	37.9	f	37.1	-2.2

Last but not least, the distribution of the von Mises stress is presented in Fig. 6 when the indentation depth is 750 nm, and the loading direction is [212]. By comparing Fig. 6(a), (c) and (e), as well as Fig. 6(b), (d) and (f), one can see that the area of the region of the von Mises stress shrinks with the increase of temperature for the cases with and without plasma effect. Moreover, the difference in the distribution of the von Mises stress with and without plasma effect is not obvious at the same temperature, indicating the limited influence of the plasma-induced dislocations on the distribution of the stress field.

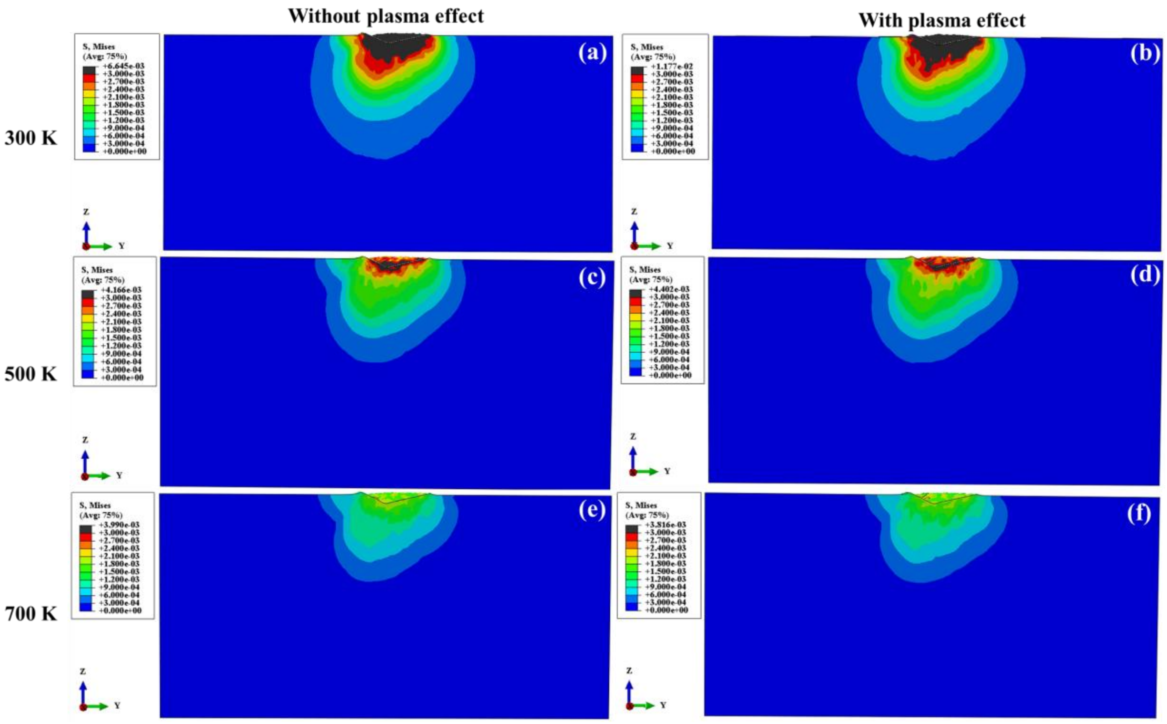

Fig. 6. The effects of plasma and temperature on the distribution of the von Mises stresses (measured in TPa). The indentation depth is 750 nm, and the loading direction is along [212].

4. Summary and conclusions

In this work, the mechanical properties of polycrystalline tungsten exposed to high-flux plasma are addressed in the temperature range of 300-700 K. By considering the limited depth of the plasma-exposed sub-surface, the NI mechanical test with a Berkovich indenter is simulated by the developed CPFEM model. Both the force-depth and hardness-depth relationships, as well as the microstructural evolution behavior are analyzed, and the main conclusions can be summarized as follows:

(1) The increase of sub-surface hardness induced by the D plasma exposure can be reliably attributed to the modification of the microstructure expressed as the increase of the dislocation density which is not homogeneous across the depth. The FEM calculations, which are based on the parameterization derived for the reference

(unexposed) material and take the dislocation density as a variable input parameter for the model, demonstrate a good agreement with the experimental data.

(2) The prediction of FEM simulations, performed to assess the response of IGP tungsten at elevated temperatures (i.e. operational temperature of the ITER divertor), shows that the concerned plasma-induced microstructural modifications do not yield to any considerable increase of hardness in the sub-surface region of 5-10 μm. Hence, we conclude that the high flux plasma exposure within the studied conditions does not impose a strong increase of hardness at operational temperature.

(3) By acting as the obstruction of gliding dislocations, the plasma-induced dislocations can, to some extent, limit the expansion of the plasticity-affected region. Whereas, the increase of temperature can effectively reduce this limitation, making the plastic zone almost be unaffected by the plasma exposure.

Acknowledgements

The views and opinions expressed herein do not necessarily reflect those of the European Commission. Z. X. acknowledges the support by the National Nature Science foundation of China (NSFC) under Contract No. 11802344 and the initial funding provided by Central South University. This project has received funding from the Euratom research and training programme 2014-2018 under grant agreement No. 755039.

References

[1] M. Rieth, S.L. Dudarev, S.M.G. de Vicente, J. Aktaa, T. Ahlgren, S. Autusch, D.E.J. Armstrong, M. Balden, N. Baluc, M.F. Barthe, W.W. Basuki, M. Battabyal, C.S. Becquart, D. Blagoeva, H. Boldyryeva, J. Brinkmann, M. Celino, L. Ciupinski, J.B. Correia, A. De Backer, C. Domain, E. Gaganidze, C. Garcia-Rosales, J. Gibson, M.R. Gilbert, S. Giusepponi, B. Gludovatzj, H. Greuner, K. Heinola, T. Hoschen, A. Hoffmann, N. Holstein, F. Koch, W. Krauss, H. Li, S. Lindig, J. Linke, C. Linsmeier, P. Lopez-Ruiz, H. Maier, J. Matejicek, T.P. Mishra, M. Muhammed, A. Munoz, M. Muzyk, K. Nordlund, D. Nguyen-Manh, J. Opschoor, N. Ordas, T. Palacios, G. Pintsuk, R. Pippan, J. Reiser, J. Riesch, S.G. Roberts, L. Romaner, M. Rosinski, M. Sanchez, W. Schulmeyer, H. Traxler, A. Urena, J.G. van der Laan, L. Veleva, S. Wahlberg, M. Walter, T. Weber, T. Weitkamp, S. Wurster, M.A. Yar, J.H. You, A. Zivelonghi, Recent progress in research on tungsten materials for nuclear fusion applications in Europe, Journal of Nuclear Materials 432(1-3) (2013) 482-500.

[2] R.A. Pitts, S. Carpentier, F. Escourbiac, T. Hirai, V. Komarov, S. Lisgo, A.S. Kukushkin, A. Loarte, M. Merola, A.S. Naik, R. Mitteau, M. Sugihara, B. Bazylev, P.C. Stangeby, A full tungsten divertor for ITER: Physics issues and design status, Journal of Nuclear Materials 438 (2013) S48-S56.
[3] T. Hirai, F. Escourbiac, V. Barabash, A. Durocher, A. Fedosov, L. Ferrand, T. Jokinen, V. Komarov, M. Merola, S. Carpentier-Chouchana, N. Arkhipov, V. Kuznetcov, A. Volodin, S. Suzuki, K. Ezato, Y. Seki, B. Riccardi, M. Bednarek, P. Gavila, Status of technology R&D for the ITER tungsten divertor monoblock, Journal of Nuclear Materials 463 (2015) 1248-1251.
[4] T. Hirai, S. Panayotis, V. Barabash, C. Amzallag, F. Escourbiac, A. Durocher, M. Merola, J. Linke, T. Loewenhoff, G. Pintsuk, M. Wirtz, I. Uytdenhouwen, Use of tungsten material for the ITER divertor, Nuclear Materials and Energy 9 (2016) 616-622.
[5] M. Merola, F. Escourbiac, R. Raffray, P. Chappuis, T. Hirai, A. Martin, Overview and status of ITER internal components, Fusion Engineering and Design 89(7-8) (2014) 890-895.
[6] W.Q. Chen, X.Y. Wang, X.Z. Xiao, S.L. Qu, Y.Z. Jia, W. Cui, X.Z. Cao, B. Xu, W. Liu, Characterization of dose dependent mechanical properties in helium implanted tungsten, Journal of Nuclear Materials 509 (2018) 260-266.
[7] J.S. Weaver, C. Sun, Y.Q. Wang, S.R. Kalidindi, R.P. Doerner, N.A. Mara, S. Pathak, Quantifying the mechanical effects of He, W and He plus W ion irradiation on tungsten with spherical nanoindentation, Journal of Materials Science 53(7) (2018) 5296-5316.
[8] J.W. Davis, V.R. Barabash, A. Makhankov, L. Plochl, K.T. Slattery, Assessment of tungsten for use in the ITER plasma facing components, Journal of Nuclear Materials 258-263 (1998) 308-312.
[9] R. Causey, K. Wilson, T. Venhaus, W.R. Wampler, Tritium retention in tungsten exposed to intense fluxes of 100 eV tritons, Journal of Nuclear Materials 266 (1999) 467-471.
[10] V. Philipps, Tungsten as material for plasma-facing components in fusion devices, Journal of Nuclear Materials 415(1) (2011) S2-S9.
[11] R. Neu, R. Dux, A. Kallenbach, T. Putterich, M. Balden, J.C. Fuchs, A. Herrmann, C.F. Maggi, M. O'Mullane, R. Pugno, I. Radivojevic, V. Rohde, A.C.C. Sips, W. Suttrop, A. Whiteford, A.U. team, Tungsten: an option for divertor and main chamber plasma facing components in future fusion devices, Nuclear Fusion 45(3) (2005) 209-218.
[12] M. Fukuda, A. Hasegawa, T. Tanno, S. Nogami, H. Kurishita, Property change of advanced tungsten alloys due to neutron irradiation, Journal of Nuclear Materials 442(1-3) (2013) S273-S276.
[13] R.A. Pitts, S. Bardin, B. Bazylev, M.A. van den Berg, P. Bunting, S. Carpentier-Chouchana, J.W. Coenen, Y. Corre, R. Dejarnac, F. Escourbiac, J. Gaspar, J.P. Gunn, T. Hirai, S.H. Hong, J. Horacek, D. Iglesias, M. Komm, K. Krieger, C. Lasnier, G.F. Matthews, T.W. Morgan, S. Panayotis, S. Pestchanyi, A. Podolnik, R.E. Nygren, D.L. Rudakov, G. De Temmerman, P. Vondracek, J.G. Watkins, Physics conclusions in support of ITER W divertor monoblock shaping, Nuclear Materials and Energy 12 (2017) 60-74.
[14] J.H. You, E. Visca, C. Bachmann, T. Barrett, F. Crescenzi, M. Fursdon, H. Greuner, D. Guilhem, P. Languille, M. Li, S. McIntosh, A.V. Mueller, J. Reiser, M. Richou, M. Rieth, European DEMO divertor target: Operational requirements and material-design interface, Nuclear Materials and Energy 9 (2016) 171-176.
[15] H. Bolt, V. Barabash, W. Krauss, J. Linke, R. Neu, S. Suzuki, N. Yoshida, A.U. Team, Materials for the plasma-facing components of fusion reactors, Journal of Nuclear Materials 329 (2004) 66-73.
[16] S. Sharafat, A. Takahashi, K. Nagasawa, N. Ghoniem, A description of stress driven bubble growth of helium implanted tungsten, Journal of Nuclear Materials 389(2) (2009) 203-212.

[17] M. Wirtz, S. Bardin, A. Huber, A. Kreter, J. Linke, T.W. Morgan, G. Pintsuk, M. Reinhart, G. Sergienko, I. Steudel, G. De Temmerman, B. Unterberg, Impact of combined hydrogen plasma and transient heat loads on the performance of tungsten as plasma facing material, Nuclear Fusion 55(12) (2015).

[18] A. Suslova, O. El-Atwani, D. Sagapuram, S.S. Harilal, A. Hassanein, Recrystallization and grain growth induced by ELMs-like transient heat loads in deformed tungsten samples, Scientific Reports 4 (2014).

[19] A. Zinovev, D. Terentyev, L. Delannay, Finite element analysis of heat load of tungsten relevant to ITER conditions, Physica Scripta T170 (2017).

[20] L. Buzi, G. De Temmerman, A.E. Huisman, S. Bardin, T.W. Morgan, M. Rasinski, R.A. Pitts, G. Van Oost, Response of tungsten surfaces to helium and hydrogen plasma exposure under ITER relevant steady state and repetitive transient conditions, Nuclear Fusion 57(12) (2017).

[21] S. Pestchanyi, I. Garkusha, I. Landman, Simulation of residual thermostress in tungsten after repetitive ELM-like heat loads, Fusion Engineering and Design 86(9-11) (2011) 1681-1684.

[22] W. Van Renterghem, A. Dubinko, A. Bakaeva, D. Terentyev, TEM investigation of the effect of He-seeding on plasma induced defects in tungsten, Journal of Nuclear Materials 508 (2018) 74-81.

[23] A.V. Dubinko, D.A. Terentyev, E.E. Zhurkin, Study of the Microstructure Induced by High-Flux Plasma via Transmission Electron Microscopy, Journal of Surface Investigation 12(4) (2018) 792-796.

[24] D. Terentyev, A. Dubinko, A. Bakaeva, G. De Temmerman, Strong sub-surface plastic deformation induced by high flux plasma in tungsten, Fusion Engineering and Design 124 (2017) 405-409.

[25] A. Dubinko, D. Terentyev, A. Bakaeva, T. Pardoen, M. Zibrov, T.W. Morgan, Effect of high flux plasma exposure on the micro-structural and -mechanical properties of ITER specification tungsten, Nuclear Instruments & Methods in Physics Research Section B-Beam Interactions with Materials and Atoms 393 (2017) 155-159.

[26] A. Dubinko, D. Terentyev, A. Bakaeva, M. Hernandez-Mayoral, G. De Temmerman, L. Buzi, J.M. Noterdaeme, B. Unterberg, Sub-surface microstructure of single and polycrystalline tungsten after high flux plasma exposure studied by TEM, Applied Surface Science 393 (2017) 330-339.

[27] D. Terentyev, A. Bakaeva, T. Pardoen, A. Favache, E.E. Zhurkin, Surface hardening induced by high flux plasma in tungsten revealed by nano-indentation, Journal of Nuclear Materials 476 (2016) 1-4.

[28] D. Terentyev, A. Dubinko, A. Bakaeva, G. De Temmerman, B. Unterberg, Microstructure and nano-hardness of single crystal tungsten exposed to high flux deuterium plasma, Physica Scripta T170 (2017).

[29] Y. Zayachuk, D.E.J. Armstrong, K. Bystrov, S. Van Boxel, T. Morgan, S.G. Roberts, Nanoindentation study of the combined effects of crystallography, heat treatment and exposure to high-flux deuterium plasma in tungsten, Journal of Nuclear Materials 486 (2017) 183-190.

[30] X. Fang, A. Kreter, M. Rasinski, C. Kirchlechner, S. Brinckmann, C. Linsmeier, G. Dehm, Hydrogen embrittlement of tungsten induced by deuterium plasma: Insights from nanoindentation tests, Journal of Materials Research 33(20) (2018) 3530-3536.

[31] X. Fang, A. Kreter, M. Rasinski, C. Kirchlechner, S. Brinckmann, C. Linsmeier, G. Dehm, Hydrogen embrittlement of tungsten induced by deuterium plasma: Insights from nanoindentation tests, Journal of Materials Research 33(20) (2018) 3530-3536.

[32] X.Z. Xiao, Q.Y. Chen, H. Yang, H.L. Duan, J.M. Qu, A mechanistic model for depth-dependent hardness of ion irradiated metals, Journal of Nuclear Materials 485 (2017) 80-89.

[33] X. Xiao, L. Yu, A hardening model for the cross-sectional nanoindentation of ion-irradiated materials, Journal of Nuclear Materials 511 (2018) 220-230.
[34] X.Z. Xiao, L. Yu, Comparison of linear and square superposition hardening models for the surface nanoindentation of ion-irradiated materials, Journal of Nuclear Materials 503 (2018) 110-115.
[35] M. Liu, C. Lu, K.A. Tieu, K. Zhou, Crystal plasticity FEM study of nanoindentation behaviors of Cu bicrystals and Cu-Al bicrystals, Journal of Materials Research 30(16) (2015) 2485-2499.
[36] W.Z. Yao, J.H. You, Berkovich nanoindentation study of monocrystalline tungsten: a crystal plasticity study of surface pile-up deformation, Philosophical Magazine 97(17) (2017) 1418-1435.
[37] G.Y. Liu, M. Song, X.L. Liu, S. Ni, S.L. Wang, Y.H. He, Y. Liu, An investigation of the mechanical behaviors of micro-sized tungsten whiskers using nanoindentation, Materials Science and Engineering a-Structural Materials Properties Microstructure and Processing 594 (2014) 278-286.
[38] W.B. Lee, Y.P. Chen, Simulation of micro-indentation hardness of FCC single crystals by mechanism-based strain gradient crystal plasticity, International Journal of Plasticity 26(10) (2010) 1527-1540.
[39] M. Saleh, Z. Zaidi, M. Ionescu, C. Hurt, K. Short, J. Daniels, P. Munroe, L. Edwards, D. Bhattacharyya, Relationship between damage and hardness profiles in ion irradiated SS316 using nanoindentation - Experiments and modelling, International Journal of Plasticity 86 (2016) 151-169.
[40] X. Xiao, D. Terentyev, A. Ruiz, A. Zinovev, A. Bakaev, E.E. Zhurkin, High temperature nano-indentation of tungsten: Modelling and experimental validation Materials Science & Engineering A 743 (2019) 106-113.
[41] A. Dubinko, Plastic Deformation of Tungsten under Fusion-Plasma Exposure Conditions Department of Applied Physics, Ghent University 2017.
[42] A. Dubinko, D. Terentyev, A. Bakaeva, K. Verbeken, M. Wirtz, M. Hernandez-Mayoral, Evolution of plastic deformation in heavily deformed and recrystallized tungsten of ITER specification studied by TEM, International Journal of Refractory Metals & Hard Materials 66 (2017) 105-115.
[43] G.J. van Rooij, V.P. Veremiyenko, W.J. Goedheer, B. de Groot, A.W. Kleyn, P.H.M. Smeets, T.W. Versloot, D.G. Whyte, R. Engeln, D.C. Schram, N.J.L. Cardozo, Extreme hydrogen plasma densities achieved in a linear plasma generator, Applied Physics Letters 90(12) (2007).
[44] H.J. Van der Meiden, R.S. Al, C.J. Barth, A.J.H. Donne, R. Engeln, W.J. Goedheer, B. De Groot, A.W. Kleyn, W.R. Koppers, N.J.L. Cardozo, M.J. Van de Pol, P.R. Prins, D.C. Schram, A.E. Shumack, P.H.M. Smeets, W.A.J. Vijvers, J. Westerhout, G.M. Wright, G.J. van Rooij, High sensitivity imaging Thomson scattering for low temperature plasma, Review of Scientific Instruments 79(1) (2008).
[45] W.C. Oliver, G.M. Pharr, Measurement of hardness and elastic modulus by instrumented indentation: Advances in understanding and refinements to methodology, Journal of Materials Research 19(1) (2004) 3-20.
[46] W.C. Oliver, G.M. Pharr, An improved technique for determining hardness and elastic-modulus using load and displacement sensing indentation experiments, Journal of Materials Research 7(6) (1992) 1564-1583.

Figure(s)
Click here to download high resolution image

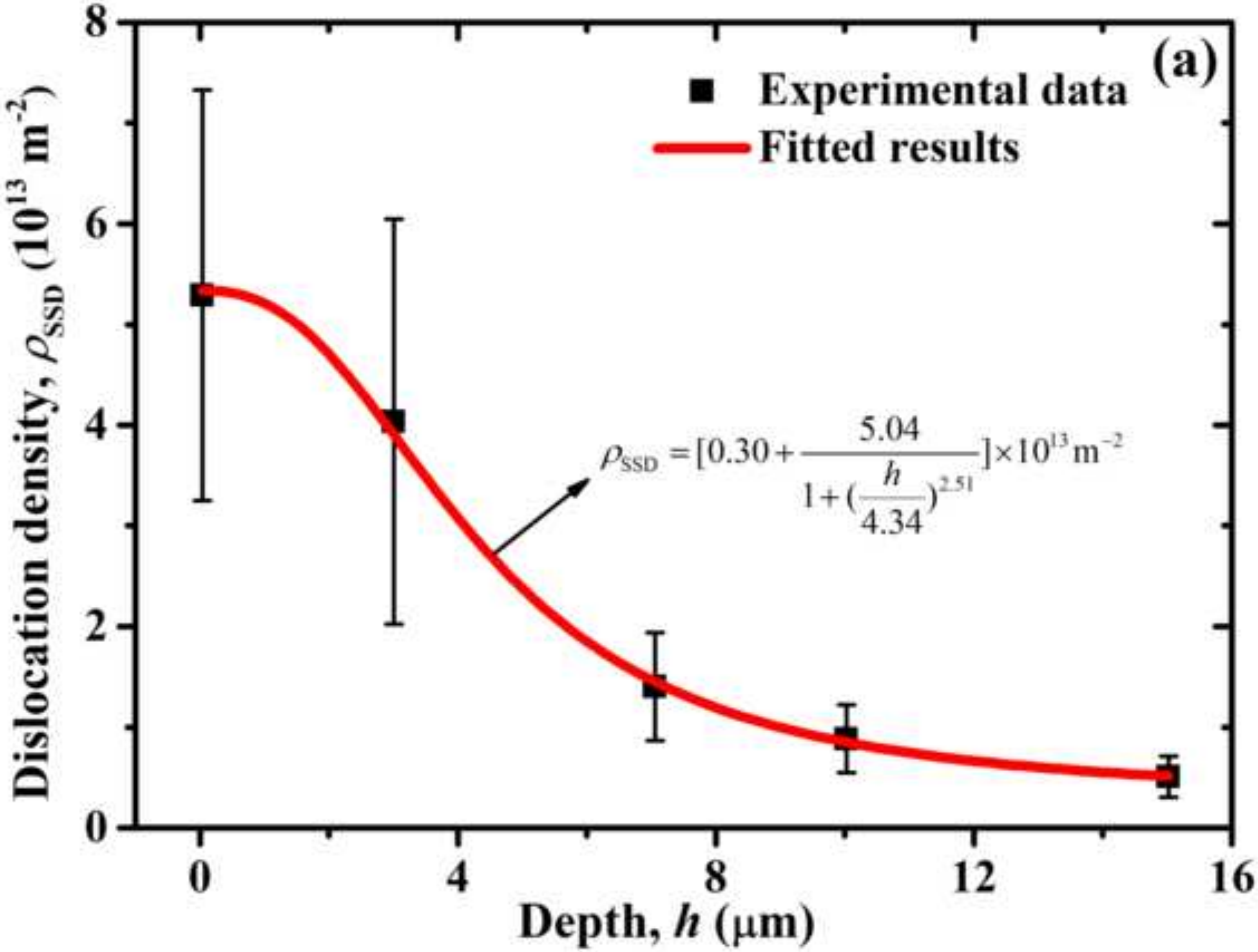

Figure(s)
Click here to download high resolution image

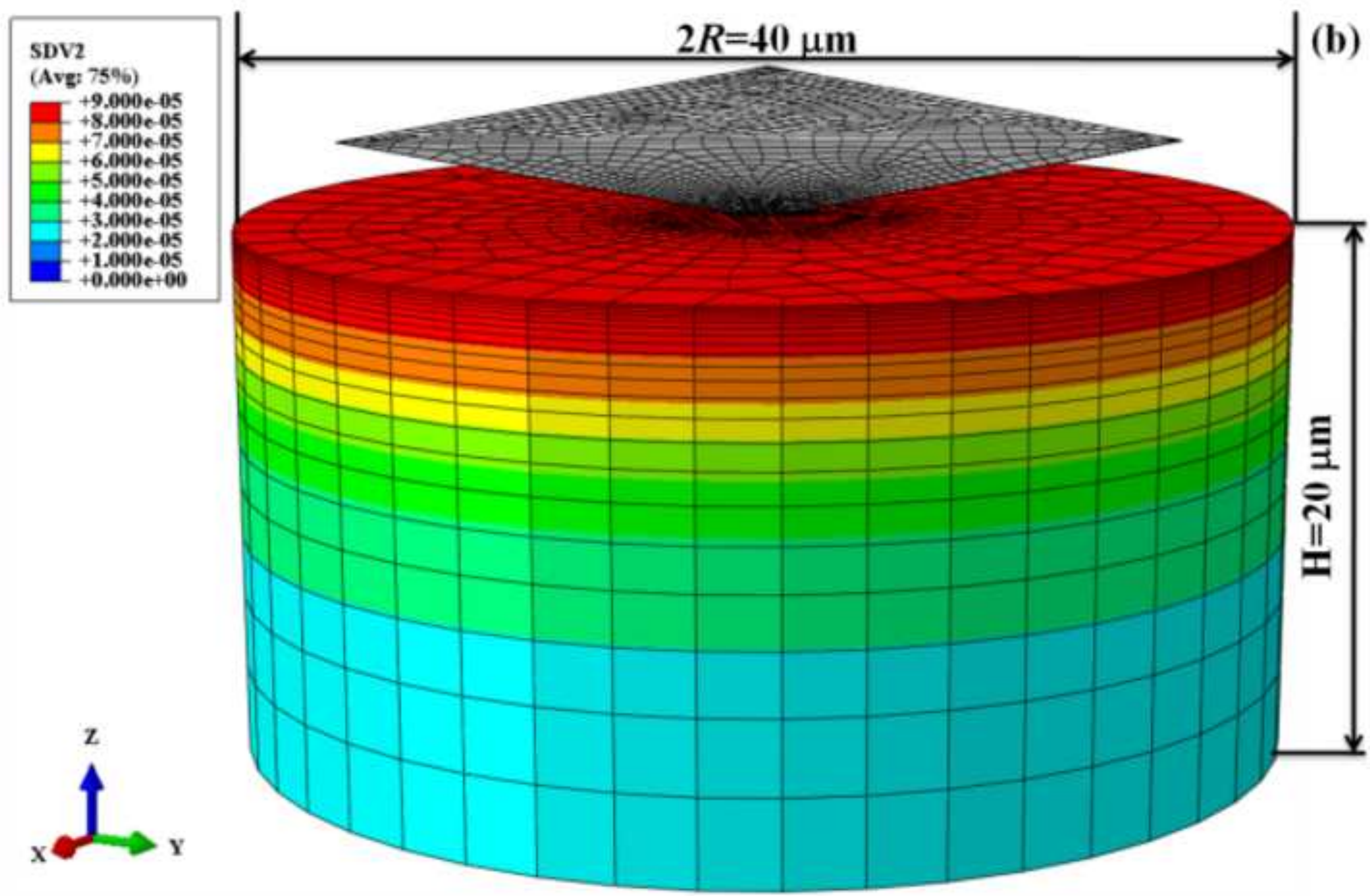

Figure(s)
Click here to download high resolution image

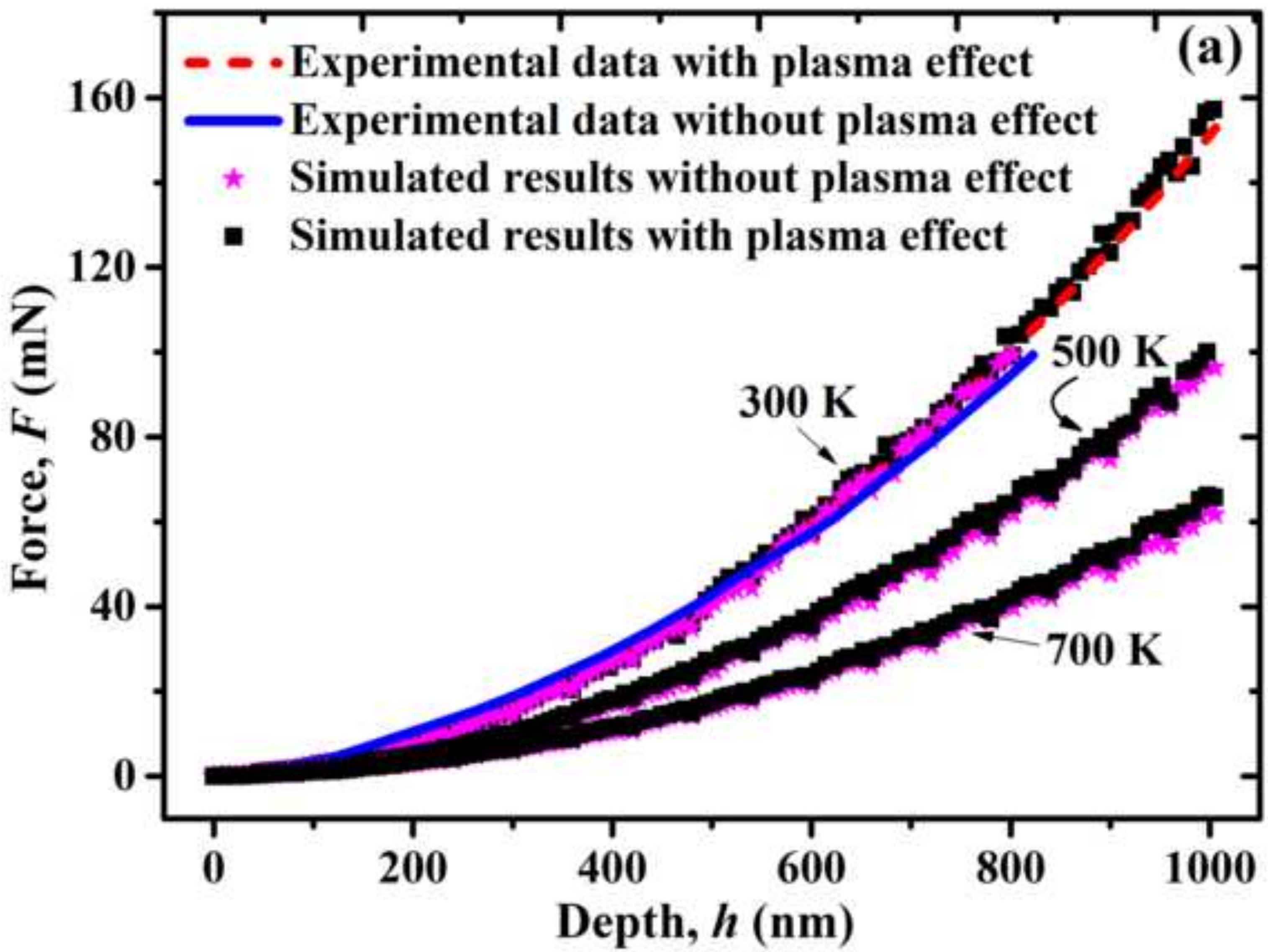

Figure(s)
Click here to download high resolution image

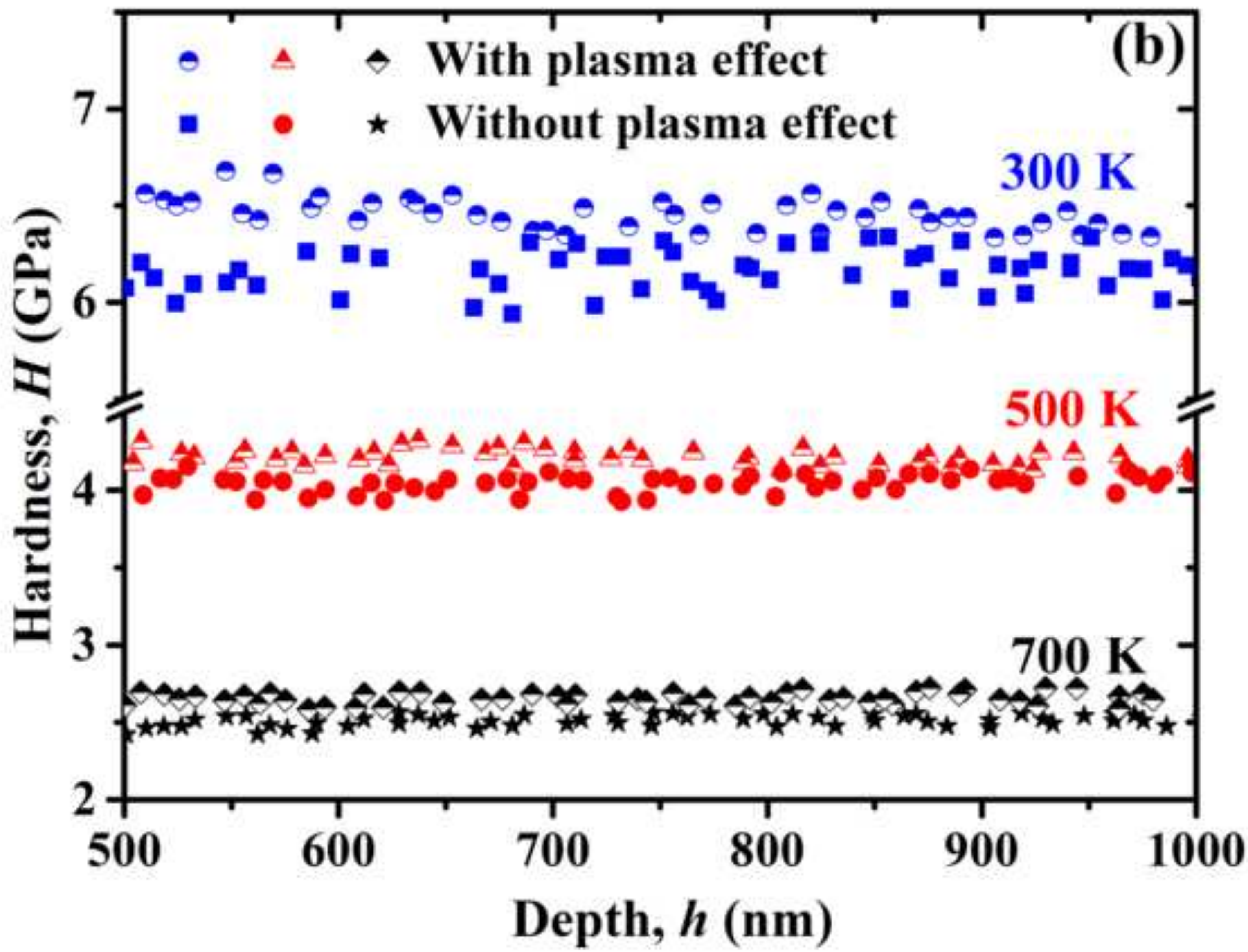

Figure(s)
Click here to download high resolution image

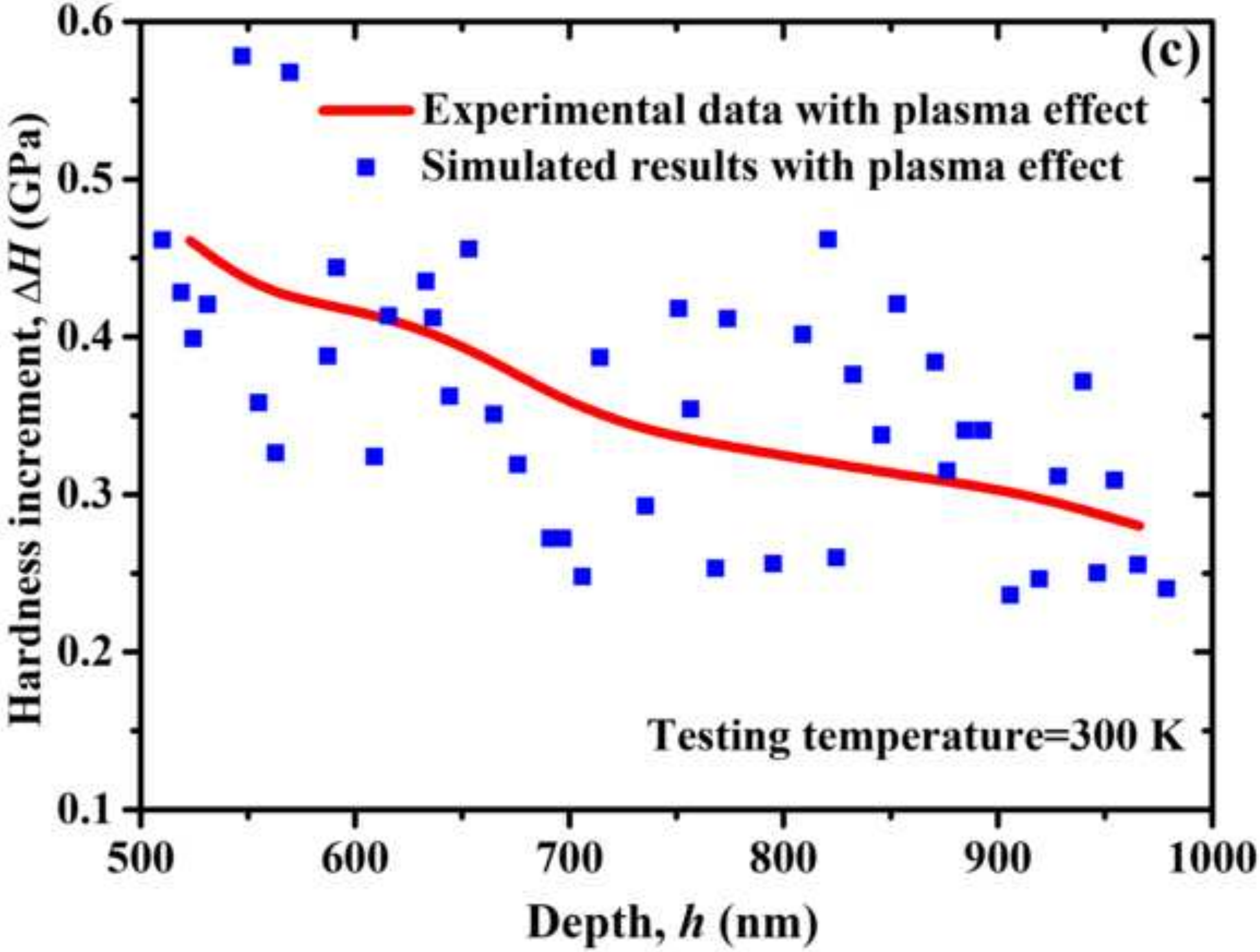

Figure(s)
Click here to download high resolution image

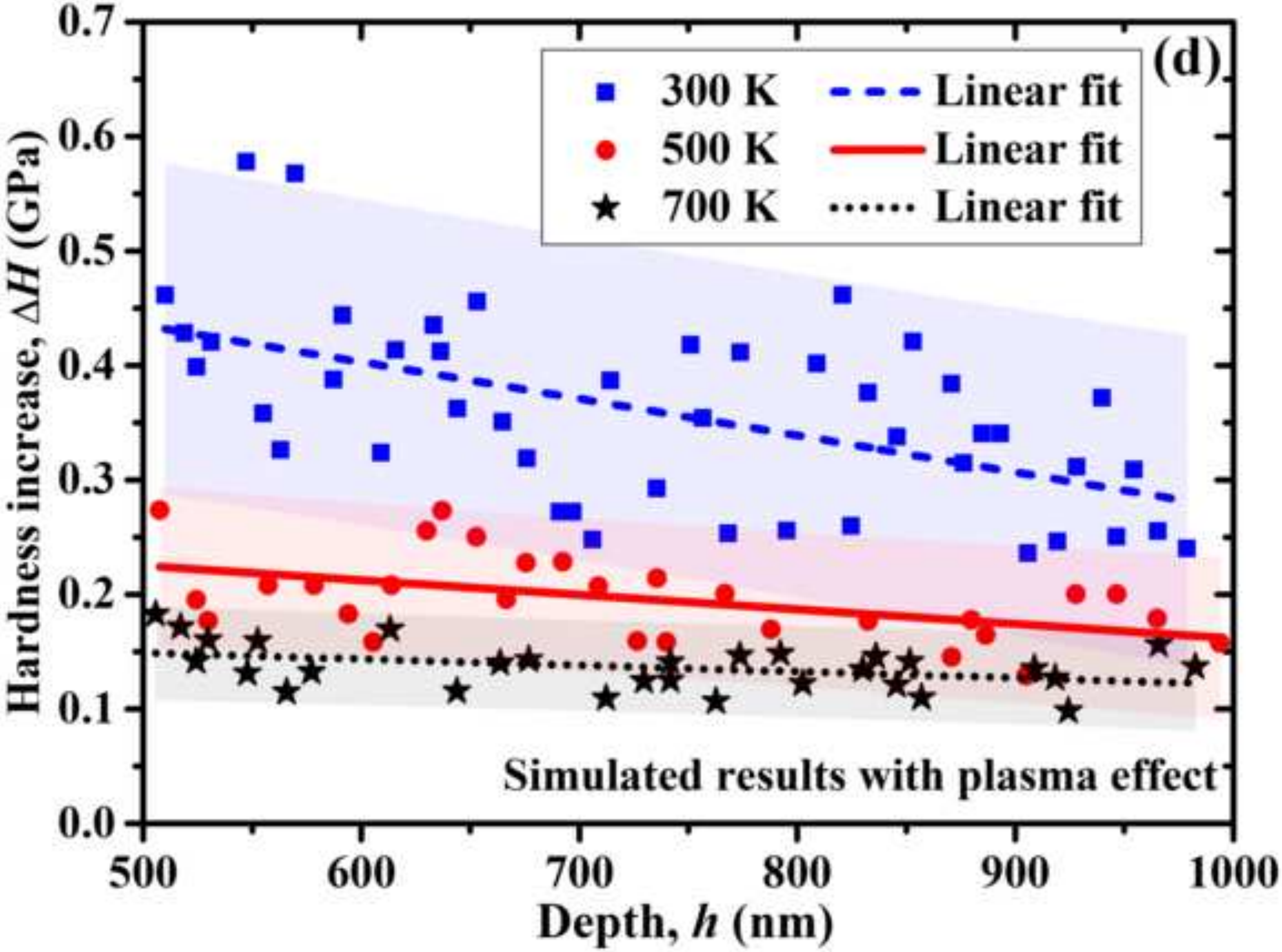

Figure(s)
Click here to download high resolution image

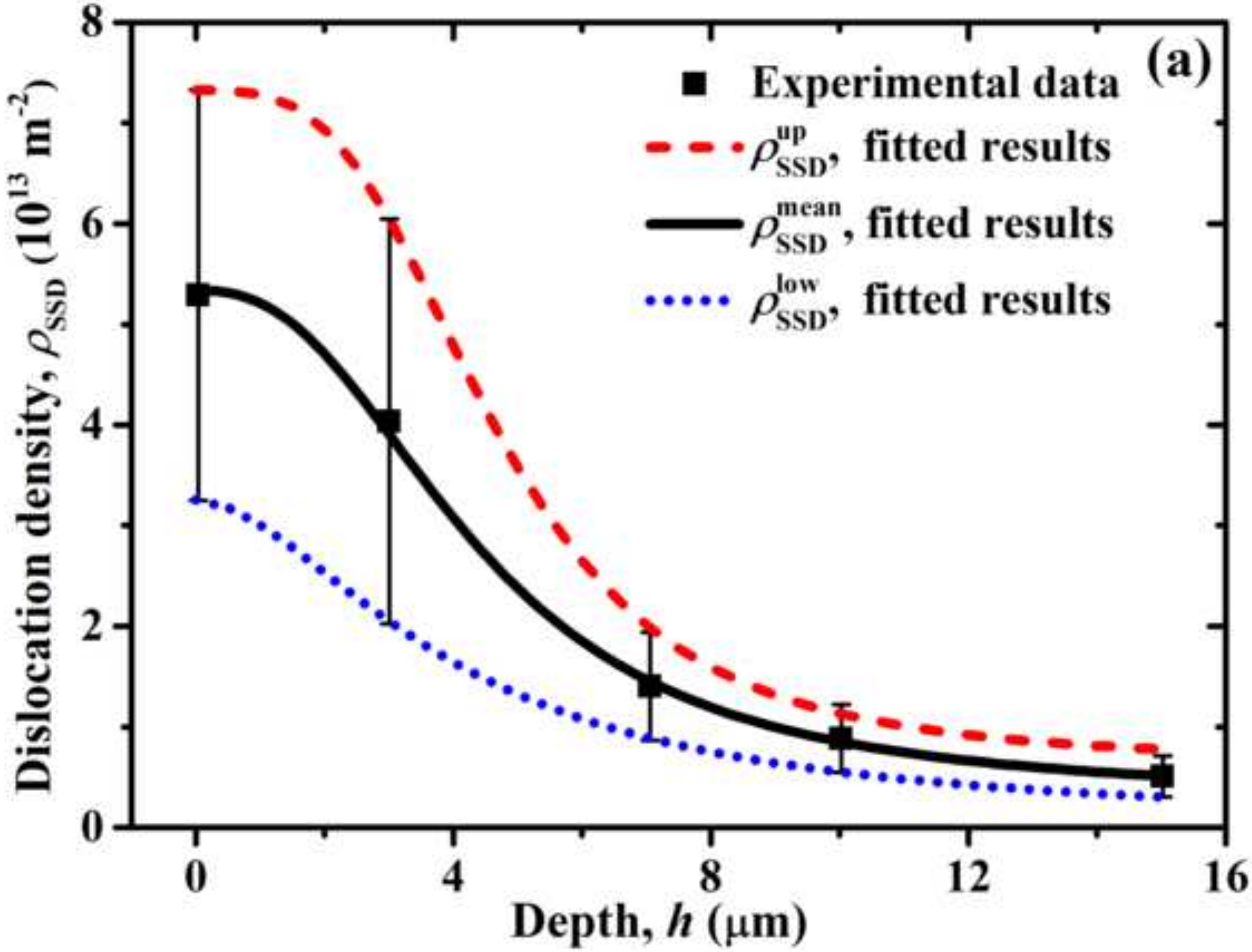

Figure(s)
Click here to download high resolution image

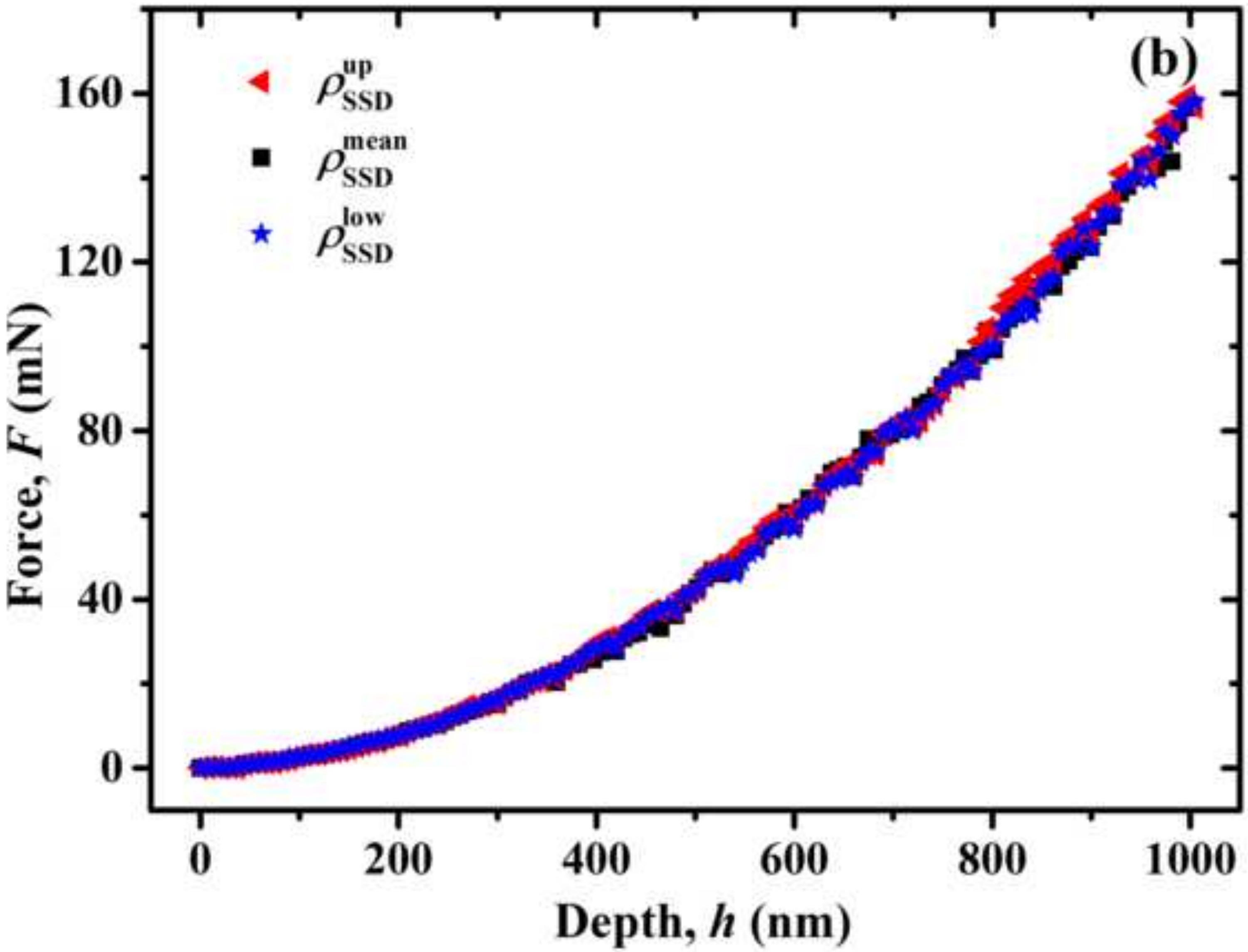

Figure(s)
Click here to download high resolution image

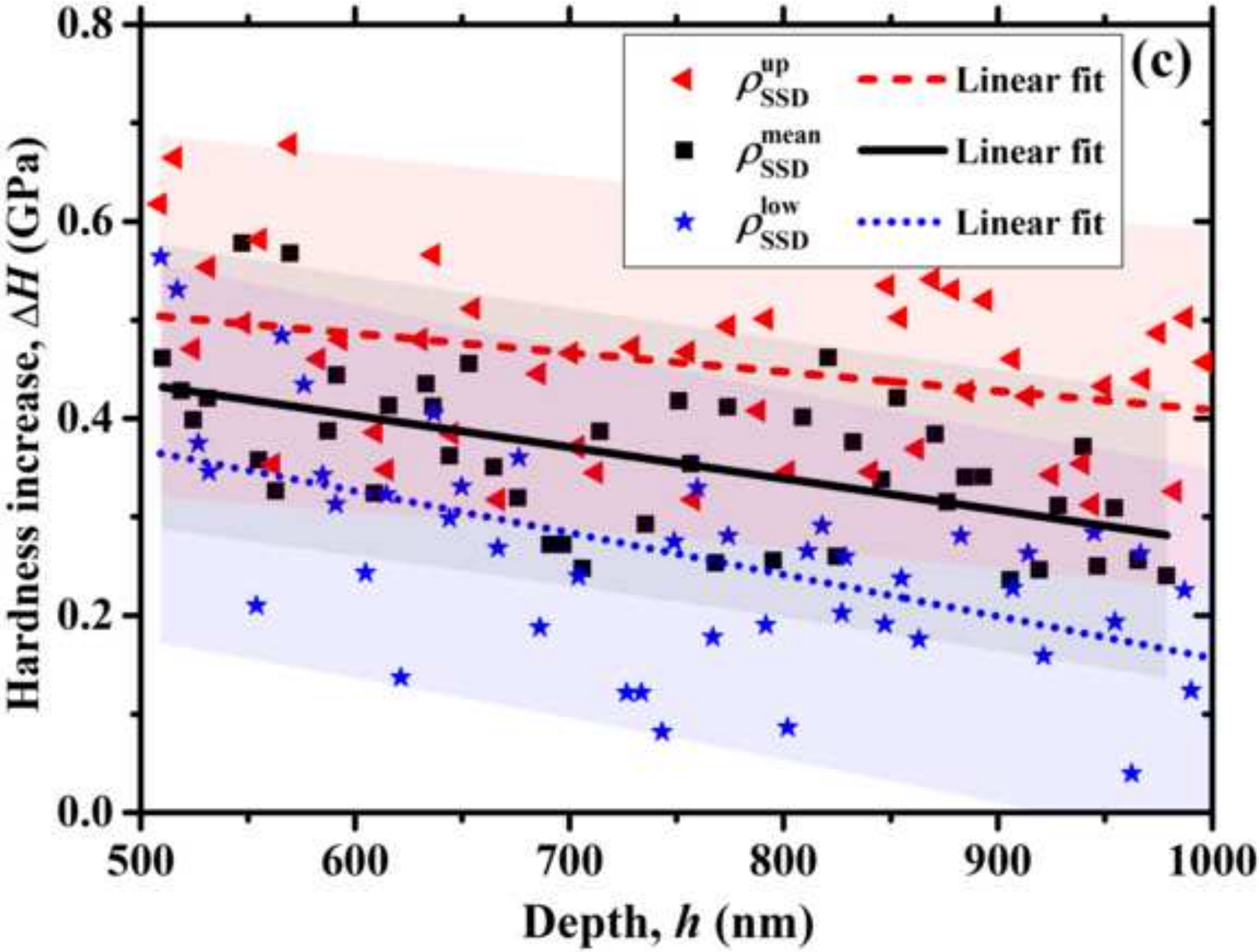

Figure(s)

Click here to download high resolution image

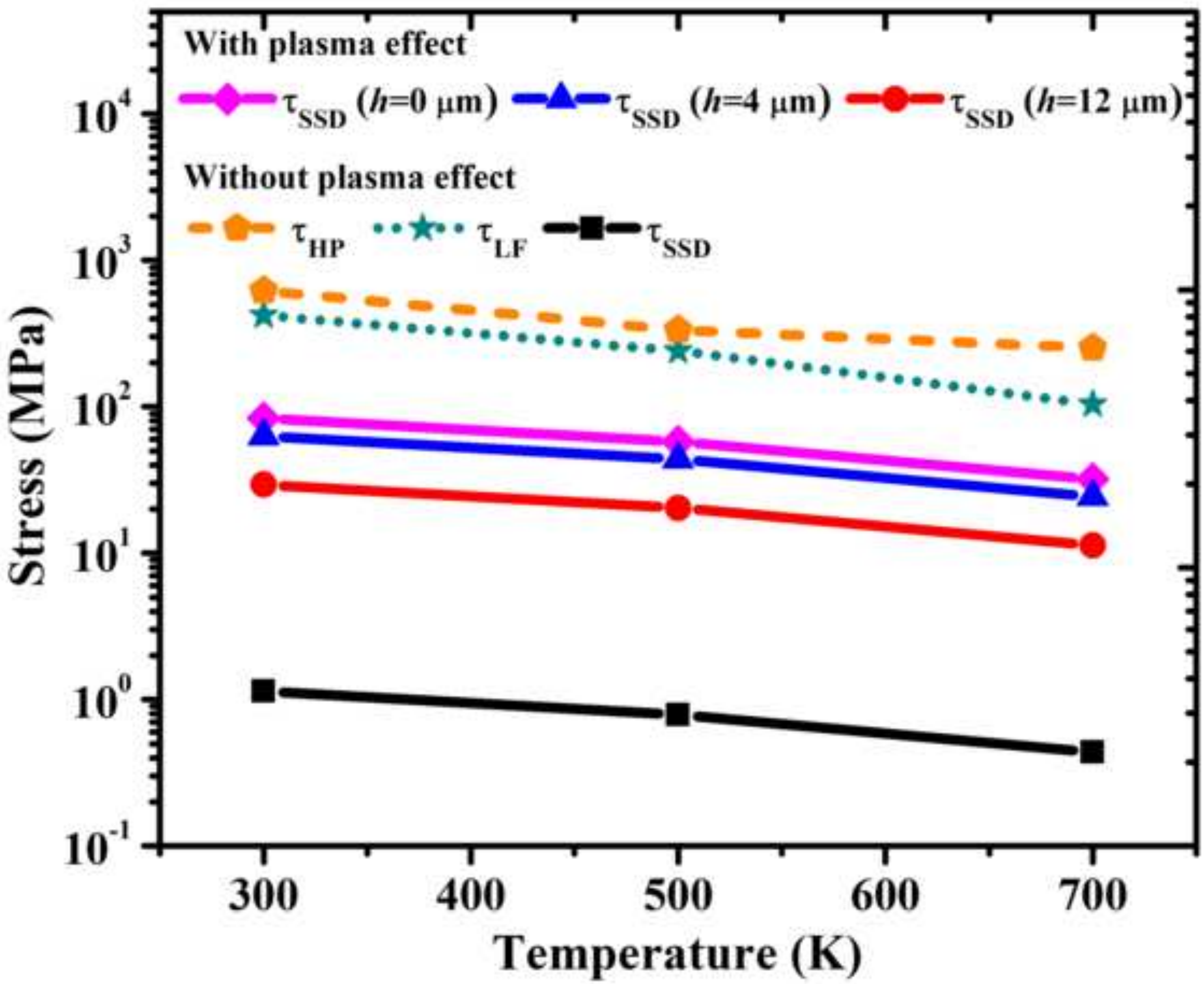

Figure(s)
Click here to download high resolution image

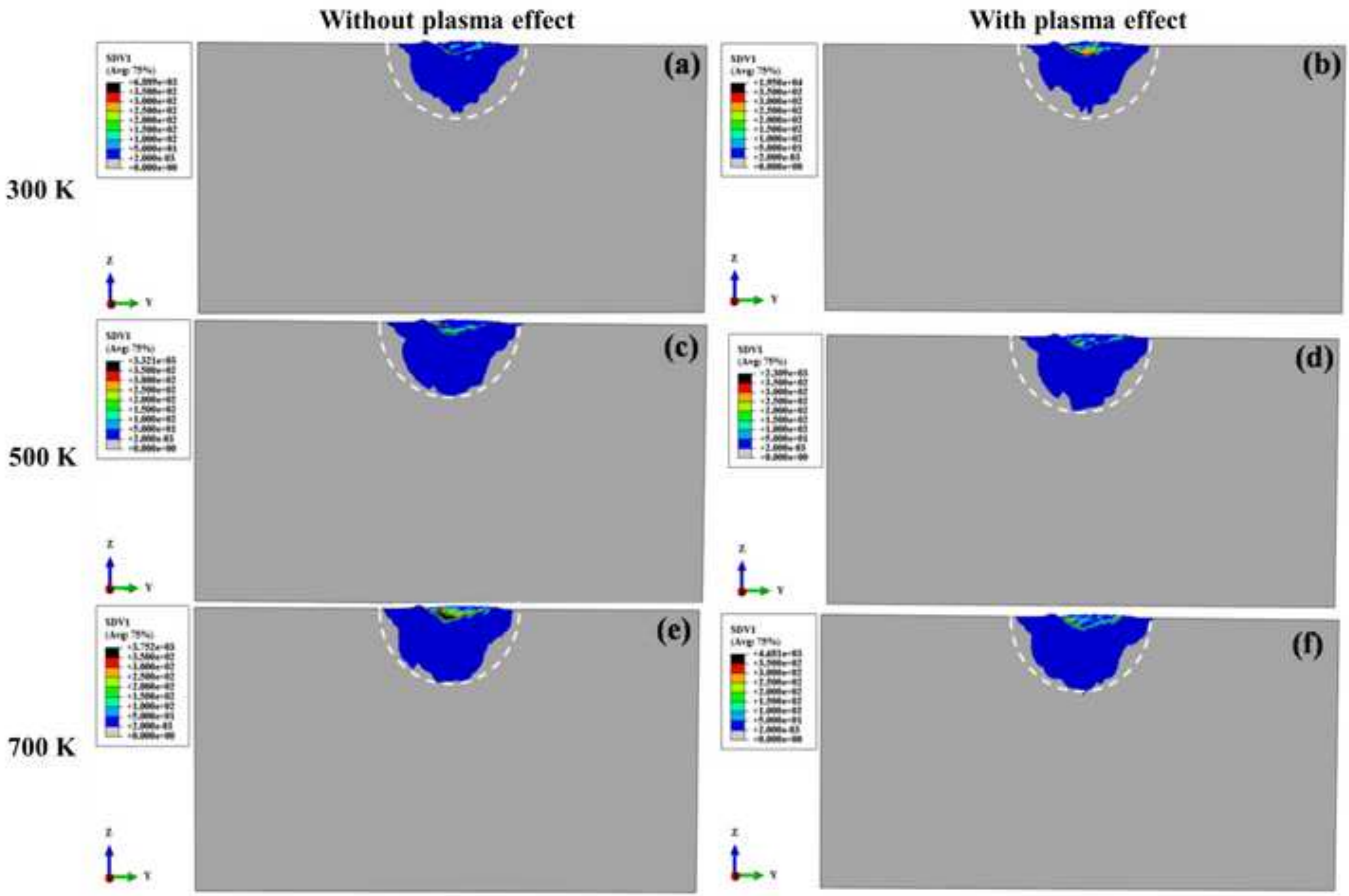

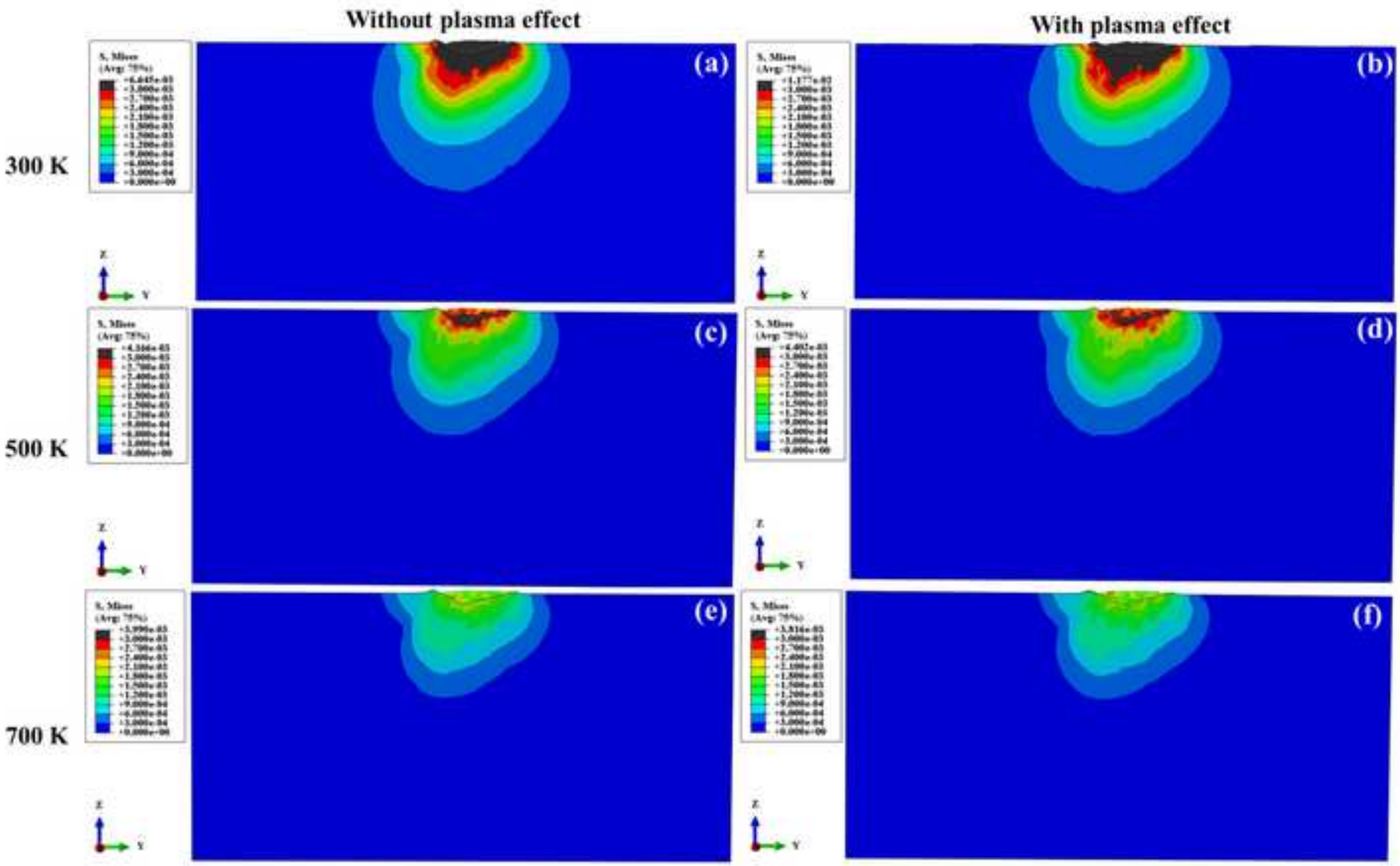
Without plasma effect
With plasma effect
300 K
500 K
700 K
(a)
(b)
(c)
(d)
(e)
(f)

Figure(s)

Figure Captions

Fig. 1. (a) The initial distribution of dislocation density in IGP W after the pure D plasma exposure at 470 K and the fluence up to 4×10^{26} D/m^2 [41]. (b) The initial distribution of τ_{SSD} at 300 K (measured in TPa) corresponding to the distribution of dislocation density as illustrated in Fig. 1(a).

Fig. 2. (a) The experimental data (lines) and simulated NI results (dots) are compared for the $F-h$ relationship of plasma-exposed IGP tungsten when the testing temperatures are 300 K, 500 K and 700 K. (b) The simulated $H-h$ relationships with and without plasma effect are compared for the different testing temperatures. (c) The $\Delta H-h$ relationship is compared between the experimental data and simulated results when the testing temperature is 300 K. (d) The simulated $\Delta H-h$ relationship is compared when the testing temperature are 300 K, 500 K and 700 K. The linear fit for each set of simulated results and 95% prediction bands are also added.

Fig. 3. (a) The dislocation density depth profile with different fitting functions for the upper boundary (ρ_{SSD}^{up}, dashed line), mean value (ρ_{SSD}^{mean}, solid line) and lower boundary (ρ_{SSD}^{low}, dotted line) of experimental data [41]. (b) The simulated $F-h$ relationship for three distributions of dislocation density, i.e. ρ_{SSD}^{up}, ρ_{SSD}^{mean} and ρ_{SSD}^{low}. (c) The simulated $\Delta H-h$ relationship for three distributions of dislocation density, i.e. ρ_{SSD}^{up}, ρ_{SSD}^{mean} and ρ_{SSD}^{low}. The linear fit for each set of simulated results and 95% prediction band are also added.

Fig. 4. The temperature and plasma effects on τ_{SSD}, τ_{LF} and τ_{HP}. For plasma-exposed tungsten τ_{SSD} is shown for the depths equal to h=0 μm, h=4 μm and h=12 μm.

Fig. 5. The effects of plasma and temperature on the distribution of PEEQ. The

indentation depth is 750 nm, and the loading direction is along [212]. The hemisphere with dashed lines is of the same radius in all six figures.

Fig. 6. The effects of plasma and temperature on the distribution of the von Mises stresses (measured in TPa). The indentation depth is 750 nm, and the loading direction is along [212].

Table(s)

Table 1. The fundamental constitutive equations for plasma-exposed tungsten with temperature effect.

Definition	Expression	Function	Description
Critical resolved shear stress (CRSS)	$\tau_{\mathrm{CRSS}}^{\alpha}(T,h)$	$\tau_{\mathrm{LF}}(T)+\tau_{\mathrm{HP}}(T)+\tau_{\mathrm{SSD}}^{\alpha}(T,h)$	Three hardening terms contribute to the CRSS in the α-th slip system
Lattice friction stress	$\tau_{\mathrm{LF}}(T)$	$\begin{cases}\tau_{\mathrm{p0}}\left[1-\sqrt{\dfrac{k_{\mathrm{B}}T}{2H_{\mathrm{k}}}\ln\left(\dfrac{\dot{\gamma}_{\mathrm{p0}}}{\dot{\varepsilon}}\right)}\right], T\le T_0\\ \tau_{\mathrm{f0}}\left[1-\dfrac{k_{\mathrm{B}}T}{2H_{\mathrm{k}}}\ln\left(\dfrac{\dot{\gamma}_{\mathrm{p0}}}{\dot{\varepsilon}}\right)\right]^2, T>T_0\end{cases}$	$\tau_{\mathrm{LF}}(T)$ indicates the thermally-activated motion of screw dislocations
Hall-Petch hardening term	$\tau_{\mathrm{HP}}(T)$	$k_{\mathrm{HP}}(T)d^{-0.5}$	$\tau_{\mathrm{HP}}(T)$ characterizes the hardening effect of grain boundaries
Dislocation hardening term	$\tau_{\mathrm{SSD}}^{\alpha}(T,h)$	$\mu(T)bh_{\mathrm{SSD}}(T)\sqrt{\rho_{\mathrm{SSD}}^{\alpha}(h)}$	$\tau_{\mathrm{SSD}}^{\alpha}(T,h)$ with plasma effect is a function of T and h
Evolution of the CRSS	$\dot{\tau}_{\mathrm{CRSS}}^{\alpha}(T,h)$	$\sum_{\beta=1}^{N_s} H^{\alpha\beta}(T,h)\lvert\dot{\gamma}^{\beta}\rvert$	Evolution of dislocation density in different slip systems contributes to the evolution of CRSS

Table 2. Fitting parameters in the expression of Eq. (1) for the upper boundary, mean value and lower boundary of experimental data [41].

	A_1 ($\times10^{13}$ m^{-2})	A_2 ($\times10^{13}$ m^{-2})	h_0 (μm)	p
$\rho_{\mathrm{SSD}}^{\mathrm{up}}$	0.64	6.68	4.64	3.31
$\rho_{\mathrm{SSD}}^{\mathrm{mean}}$	0.30	5.03	4.34	2.51
$\rho_{\mathrm{SSD}}^{\mathrm{low}}$	0.03	3.23	4.00	1.79

Table 3. The area of the PEEQ region (S_{PEEQ}) as illustrated in Fig. 5.

Reference		Plasma-exposed		Relative difference, %
Fig. 5	S_{PEEQ} (μm^2)	Fig. 5	S_{PEEQ} (μm^2)	
a	28.9	b	26.1	-10.7
c	35.9	d	34.8	-3.1
e	37.9	f	37.1	-2.2